Revisiting the experiment of a free-surface resonance of a liquid in a vibration tank using a nonlinear fluid–structure computational model

Quentin Akkaoui, Evangéline Capiez-Lernout, Christian Soize, Roger Ohayon

Revisiting the experiment of a free-surface resonance of a liquid in a vibration tank using a nonlinear fluid-structure computational model

Q. Akkaoui[a], E. Capiez-Lernout[a], C. Soize[a,*], R. Ohayon[b]

[a] *Université Paris-Est Marne-la-Vallée, Laboratoire Modélisation et Simulation Multi Echelle (MSME) UMR 8208 CNRS, 5 boulevard Descartes, Marne-La-Vallée 77454, France*

[b] *Conservatoire National des Arts et Métiers (CNAM), Structural Mechanics and Coupled Systems Laboratory, 2 rue Conté, Paris 75003, France*

Abstract

Using an advanced nonlinear fluid-structure reduced-order computational model, this work revisits and explains a resonance of the free surface of water contained in a thin elastic cylindrical tank, which was experimentally exhibited by Lindholm, 1962 and Abramson, 1966. The proposed simulation model allows the experimental setup to be reproduced. The structure undergoes large displacements and large deformations (geometrical nonlinear effects of the structure) that play an important role on the liquid vibrations. The experimental setup is simulated using a large-scale numerical model of the elastic cylindrical tank partially filled with water that is considered as a compressible fluid and that takes into account surface tension and sloshing effects. The results show that for a frequency external excitation in the frequency band $[500, 2{,}500]\,Hz$ of the fluid-structure system, unexpected high-amplitude sloshing vibrations are observed in the frequency band $[0, 150]\,Hz$. The observed phenomenon, which cannot be reproduced with a linear fluid-structure model, is explained by the transfer of the vibrational energy from the frequency band of excitation into a low-frequency band (and then exciting the first sloshing modes) by a non-direct coupling mechanism between the structural modes and the sloshing modes.

Keywords: Fluid-structure interactions, Geometric structural nonlinearities, Vibrations, Reduced-order model, Sloshing, Capillarity

1. Introduction

This paper deals with a computational study of a fluid-structure system that proposes an explanation to an unusual sloshing resonance observed in an experimental investigation of a vibrating elastic tank partially filled with water, exhibited and investigated in (Lindholm et al., 1962; Abramson et al., 1966). The experiments performed in (Lindholm et al., 1962) were first designed to quantify the effects of an internal liquid on the breathing frequencies of a circular cylindrical thin-walled shell. During these experiments, an *unexpected behavior* was observed when the structure were subjected to a high-frequency excitation of small amplitude. The unusual results obtained in this first experiment were then investigated in further details by (Abramson et al., 1966). Indeed, *it was observed that a totally unexpected coupling between low-frequency liquid free-surface oscillation and high-frequency shell-wall vibration could occur for a wide range of parameter* (cited from (Abramson et al., 1966)). This result is all the more unexpected as the frequency separation between the first eigenfrequencies of the sloshing modes and the first structural modes is of order 100. A discussion on these results is proposed in these papers, which suggests that this unexpected behavior would be based on several *unusual characteristics that are not explained readily on the basis of existing theory* (cited from (Abramson et al., 1966)). These authors concluded that the source of such coupling could possibly come from a nonlinear coupling between the liquid and the structure for which the source of nonlinearities would not be precisely known. A first attempt for explaining this unexpected phenomenon has been carried out by (Chu and Kana, 1967) using an analytical approach with a linear theory for the structure and a nonlinear one for the free surface of

*Corresponding author

Email address: christian.soize@u-pem.fr (C. Soize)

the liquid. These authors conclude that *exact quantitative comparisons of theory and experiments may required a more complicated system*. In this paper, an alternative is proposed for explaining the observed phenomenon using a nonlinear structure (geometrical nonlinearities) and a linear compressible liquid (acoustic fluid) with sloshing and capillarity effects using a large-scale computational model. The observed experimental results are simulated and the mechanisms of this unexpected free-surface response is detailed, which constitutes the novelty of this work.

Theory and applications of liquid sloshing in elastic structures has been investigated in literature (see for example, (Paidoussis, 1998; Dodge, 2000; Ibrahim, 2005; Faltinsen and Timokha, 2009; Moiseyev and Rumyantsev, 2012)). The effects of surface tension (capillarity effects) in a rigid structure has also been analyzed (see for instance, (Finn, 2001, 2006; Finn and Luli, 2007)). On the computational level, variational formulations, computational models, and reduced-order models concerning vibroacoustics and fluid-structure interactions can be found, for instance, in (Morand and Ohayon, 1995; Ohayon and Soize, 1997, 2014, 2015; Bermúdez et al., 2003; Schotté and Ohayon, 2005, 2013; Farhat et al., 2013; Hambric et al., 2016).

The effects of the geometrical nonlinearities of structures containing liquids have been studied in order to quantify the influence of a fluid on the large amplitude motion of the structure (Dowell, 1998; Amabili and Paıdoussis, 2003; Amabili, 2008; Strand and Faltinsen, 2017; Alijani and Amabili, 2014). For example, many experimental studies are available for large amplitude vibrations of thin shells partially filled with liquids such as the ones proposed by (Olson, 1965; Leissa, 1973; Chen and Babcock, 1975; Chiba, 1992; Koval'chuk and Lakiza, 1995) and also by (Carra et al., 2013) in which the experimental study that is presented could be used as a test case for future nonlinear fluid-structure interaction problem. However, to the best knowledge of the authors, only the Chu-Kanna work (Chu and Kana, 1967) proposed an explanation of this *unusual* phenomenon put in evidence in (Lindholm et al., 1962; Abramson et al., 1966; Abramson and Kana, 1970), by using a linear structure coupled with a nonlinear free-surface effects of the liquid. The analysis of these four last references led us to consider the nonlinear effect of the structure, which was suggested but not investigated by these authors, coupled with a linear fluid. In order to quantify these effects, we have used a formulation that allows for taking into account the nonlinear geometric effects of the structure, while considering a linear formulation for the internal liquid in presence of sloshing and capillarity effects. This paper presents a numerical simulation of the experimental setup, using a large-scale computational model based on the formulation (Ohayon and Soize, 2015, 2016) and gives an alternative more accurate explanation of the phenomenon observed during the experiments (Lindholm et al., 1962; Abramson et al., 1966).

This experimental setup is a tank that is partially filled with a compressible liquid (acoustic fluid) that has a free surface. The whole system is submitted to earth gravity field inducing sloshing of the free surface. The computational model of the coupled system is constructed using the finite element method (Zienkiewicz et al., 1977). This computational model allows for taking into account the geometrical nonlinearities of the structure (Amabili and Paıdoussis, 2003; Wriggers, 2008; Crisfield et al., 2012; Belytschko et al., 2013). A nonlinear reduced-order model (ROM) allowing for considerably reducing the computational cost is built. Such computational ROMs adapted to fluid-structure interactions have been extensively studied these last two decades. The method of proper orthogonal decomposition (POD) has been widely used to construct a ROM, for example by (Amabili et al., 2003; Amabili and Touzé, 2007; Ballarin and Rozza, 2016). In this paper, we use the ROM proposed by (Ohayon and Soize, 2015, 2016), which consists in projecting the equations of the model onto a basis constituted of the modal bases issued from each physical subset of the fluid-structure system, for the following reasons. (i) A better understanding of the couplings between each part of the fluid-structure system can be done. (ii) It allows for filtering the eigenfrequencies of the different physical subsets of the system; it is well known that the frequency gap between the (usually low-frequency) sloshing resonances and the (usually high-frequency) elastic and acoustic resonances is huge; this means that if we were to build a global reduced-order basis, we would have to compute an untractable number of (weakly energetics) sloshing eigenmodes before reaching any acoustic or elastic eigenmodes. (iii) The computation of a global reduced-order projection basis would induce some difficulties related to the non-symmetric global formulation of the coupled problem. (iv) Such ROM allows for being predictive with a reasonable computational time (Ohayon, 2004; Ohayon and Soize, 2014).

As shown in (Ohayon and Soize, 2016), the modal bases are computed by solving three different generalized eigenvalue problems: the first one being related to the elastic structure in presence of the liquid, considered as incompressible; the second one being related to the compressible liquid in a rigid container; the third one being related to the free surface in presence gravity field and with surface tension effects. In addition, the computation of the reduced-order bases exhibits major difficulties in terms of computational cost when studying a large-scale fluid-structure model

due (i) to the high flexural motion of the thin-walled cylinder and (ii) to the free surface. These difficulties are circumvented by using the algorithms presented in (Akkaoui et al., 2018).

The outline of the paper is as follows. Section 2 deals with a summary of the computational model. Section 3 is devoted to the numerical simulation of the experimental setup. The dimensions of the physical system is described, as well as the strategy used to computationally reproduce the experimental boundary conditions. A modal characterization is presented to highlight the frequency separation between the sloshing resonances and the elastic resonances. A partial validation of the computational model is performed by comparing the eigenfrequencies of the tank with the experimental ones. We then end up by showing the forced responses of the coupled system highlighting the geometrical nonlinearities effects on the dynamical behavior of the system and in particular on the amplitude of the free surface motion.

2. Summarizing the computational model used for the numerical simulations

In this section, we summarize the construction of the computational model detailed in (Ohayon and Soize, 2016), which will be used for simulating the experimental setup.

2.1. Boundary value problem for the nonlinear fluid-structure problem

The fluid-structure system is considered to be taken in its *reference configuration* defined in Figure 1. The structure occupies a bounded volume Ω_U and is taken in its natural state without prestresses. The structure contains a liquid occupying a bounded domain Ω_P. The liquid is modeled by a linear dissipative compressible fluid (dissipative acoustic fluid, see Ohayon and Soize (2014)), which means that the vibrational motion of the liquid is assumed to be small enough. Gravitational and surface tension effects are taken into account but internal gravity waves are neglected. It should be noted that the geometry of Ω_P is obtained by a first computation allowing the static equilibrium position of the free surface of the liquid to be found, due to the presence of capillarity effects.

The boundary of Ω_P, assumed to be smooth enough, is denoted as $\partial\Omega_P = \Gamma_L \cup \gamma \cup \Gamma$ (with $\Gamma_L \cap \gamma = \varnothing$, $\Gamma \cap \gamma = \varnothing$, and $\Gamma_L \cap \Gamma = \varnothing$), where Γ_L is the fluid-structure interface, Γ is the free surface of the liquid and γ is the contact line between the structure and the liquid. The boundary of Ω_U, assumed to be smooth enough, is denoted as $\partial\Omega_U = \Gamma_0 \cup \Gamma_E \cup \Gamma_L \cup \gamma \cup \Gamma_G$ where Γ_0 is a part of the boundary in which there is the Dirichlet condition $\mathbf{u} = 0$, where Γ_E is the external surface of the structure and Γ_G is the structure internal wall without contact with the liquid. The structure is submitted to a given body force field $\mathbf{b}$ in Ω_U and to a given surface force field $\mathbf{f}$ on Γ_E. The external unitary normals to $\partial\Omega_U$ and $\partial\Omega_P$ are written $\mathbf{n}^u$ and $\mathbf{n}$. Let $\boldsymbol{\nu}$ and $\boldsymbol{\nu}_L$ be the external unit normals to γ belonging respectively to the tangent plane to Γ and to the tangent plane to Γ_L.

Let $\mathbf{x} = (x_1, x_2, x_3)$ be the generic point in a Cartesian reference system $(\mathbf{O}, \mathbf{e}_1, \mathbf{e}_2, \mathbf{e}_3)$. The gravity vector is $\mathbf{g} = -g\,\mathbf{e}_3$ with g the gravitational constant. The boundary value problem is expressed in terms of the structural displacement field $\mathbf{u}(\mathbf{x}, t)$, of the internal pressure field $p(\mathbf{x}, t)$, and of the normal displacement field of the free surface $\eta(\mathbf{x}, t)$. From here on, in order to simplify the notations, the convention for summation over repeated Greek and Latin indices is considered and parameters $\mathbf{x}$ and t are removed if there is no possible confusion. Let $a(\mathbf{x}, t)$ be a given function, the following notations are used : $a_{,j} = \partial a/\partial x_j$, $\dot{a} = \partial a/\partial t$, and $\ddot{a} = \partial^2 a/\partial t^2$.

The nonlinear boundary value problem in $(p, \eta, \mathbf{u})$ is written as,

$$\frac{1}{\rho_0 c_0^2}\,\ddot{p} - \frac{\tau}{\rho_0}\nabla^2\dot{p} - \frac{1}{\rho_0}\nabla^2 p = 0 \quad \text{in } \Omega_P\,, \tag{1}$$

$$\left(1 + \tau\frac{\partial}{\partial t}\right)\frac{\partial p}{\partial \mathbf{n}} = -\rho_0\,\ddot{\mathbf{u}}\cdot\mathbf{n} \quad \text{on } \Gamma_L\,, \tag{2}$$

$$\left(1 + \tau\frac{\partial}{\partial t}\right)\frac{\partial p}{\partial \mathbf{n}} = -\rho_0\,\ddot{\eta} \quad \text{on } \Gamma\,, \tag{3}$$

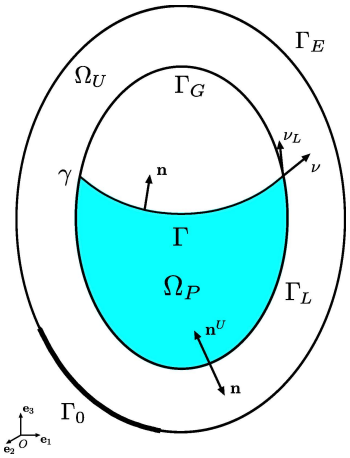

Figure 1: Reference configuration of the coupled fluid-structure system

$$p = \rho_0\,\eta\,g\,(\mathbf{e}_z\cdot\mathbf{n}) - \sigma_\Gamma\left\{\left(\frac{1}{R_1}+\frac{1}{R_2}\right)\eta + \nabla^2_\Gamma\eta\right\} \quad \text{on } \Gamma\,, \tag{4}$$

$$\frac{\partial\eta}{\partial\boldsymbol{\nu}} = c_\eta\,\eta + \mathcal{J}\,\mathbf{u} \quad \text{on } \gamma\,, \tag{5}$$

$$\rho_S\,\ddot{\mathbf{u}} - \mathrm{div}\,(\mathbb{F}\cdot\mathbb{S}) = \mathbf{b} \quad \text{in } \Omega_U\,, \tag{6}$$

$$\mathbf{u} = 0 \quad \text{on } \Gamma_0\,, \tag{7}$$

$$(\mathbb{F}\cdot\mathbb{S})\cdot\mathbf{n}^u = \mathbf{f} \quad \text{on } \Gamma_E\,, \tag{8}$$

$$(\mathbb{F}\cdot\mathbb{S})\cdot\mathbf{n}^u\,d\Gamma_L = p\,\mathbf{n}^u\,d\Gamma_L - \sigma_\Gamma\,(\mathcal{J}'\eta)\,d\mu_\gamma \quad \text{on } \Gamma_L\,, \tag{9}$$

in which the tensor $\mathbb{F}$ is the deformation gradient tensor defined in Ω_U by

$$\mathbb{F}_{ij} = \delta_{ij} + u_{i,j}\,, \tag{10}$$

where δ_{ij} denotes the Kronecker symbol such that $\delta_{ij} = 1$ if $i = j$ and $\delta_{ij} = 0$ otherwise. In Eq. (10), the tensor $\mathbb{S}$ is the second Piola-Kirchhoff symmetric tensor in the reference configuration written as

$$\mathbb{S}_{ij} = \mathbf{a}_{ijk\ell}\,\mathbb{E}_{k\ell} + \mathbf{b}_{ijk\ell}\,\frac{d\,\mathbb{E}_{k\ell}}{dt}\,, \tag{11}$$

where the tensors $\mathbf{a}_{ijk\ell}$ and $\mathbf{b}_{ijk\ell}$ are fourth-order real tensors, verifying the symmetry and positiveness properties and where the Green-Lagrange strain tensor is written as

$$\mathbb{E}_{k\ell} = \frac{1}{2}\left(u_{k,\ell} + u_{\ell,k} + u_{m,k}\,u_{m,\ell}\right)\,. \tag{12}$$

In Eqs. (1) to (3), ρ_0 is the constant mass density of the homogeneous liquid, c_0 is the constant speed of sound, and τ is the constant coefficient that characterizes the dissipation in the internal liquid. In Eqs. (4) and (5), σ_Γ is the surface tension coefficient, R_1 and R_2 are the main curvature radii of the free-surface, and c_η is the contact angle coefficient.

In Eq. (6), ρ_S is the constant mass density of the structure. Equations (4) and (9) correspond to the contact angle between the elastic structure and the free surface of the liquid in which the operator $\mathcal{J}$ is such that

$$\mathcal{J}\,\mathbf{u} = E\,\mathbf{u}\cdot\mathbf{n}^u - \frac{\partial(\mathbf{u}\cdot\mathbf{n}^u)}{\partial\boldsymbol{\nu}_L}\,, \tag{13}$$

in which E a real coefficient. In Eq. (9), $d\mu_\gamma$ is a real measure on Γ_L such that $\int_{\Gamma_L} f(\mathbf{x})\,d\mu_\gamma(\mathbf{x}) = \int_\gamma f(\mathbf{x})\,d\gamma(\mathbf{x})$ (this means that the support of measure $d\mu_\gamma$ is γ), and the term $(\mathcal{J}'\eta)\,d\mu_\gamma$ is defined on Γ_L by algebraic duality of the term $\mathcal{J}\,\mathbf{u}$ defined on γ.

2.2. Nonlinear computational model

Let n_p, n_h, and n_u be the number of degrees of freedom related to the fluid, to the free surface, and to the structure, issued from the finite element discretization of the system. We then denote by $\mathbf{P}$, $\mathbf{H}$, and $\mathbf{U}$ the $\mathbb{R}^{n_p}$-vector, $\mathbb{R}^{n_h}$-vector, and $\mathbb{R}^{n_u}$-vector corresponding to the finite element discretization of the fields $p(\mathbf{x},t)$, $\eta(\mathbf{x},t)$, and $\mathbf{u}(\mathbf{x},t)$. The computational finite element model of the fluid-structure system is then written as

$$[M]\,\ddot{\mathbf{P}} + [D]\,\dot{\mathbf{P}} + [K]\,\mathbf{P} - [C_{p\eta}]^T\,\ddot{\mathbf{H}} - [C_{pu}]^T\,\ddot{\mathbf{U}} = 0\,, \tag{14}$$

$$[C_{p\eta}]\,\mathbf{P} + [K_{gc}]\,\mathbf{H} + [C_{\eta u}]\,\mathbf{U} = 0\,, \tag{15}$$

$$[C_{pu}]\,\mathbf{P} + [C_{\eta u}]^T\,\mathbf{H} + [M_u]\,\ddot{\mathbf{U}} + [D_u]\,\dot{\mathbf{U}} + [K_u]\,\mathbf{U} + \mathbf{F}_{NL}(\mathbf{U}) = \mathbf{F}_u\,. \tag{16}$$

In Eq. (14), the $(n_p \times n_p)$ symmetric positive-definite matrix $[M]$ is the fluid "mass" matrix. The $(n_p \times n_p)$ positive-semidefinite matrices $[K]$ and $[D] = \tau\,[K]$ are the "stiffness" and "damping" matrices of the liquid. In Eq. (15), the $(n_h \times n_h)$ symmetric positive-definite matrix $[K_{gc}]$ is the matrix related to the sloshing/capillarity effects on the free surface. In Eq. (16), only the linear part of the damping forces are kept and are represented by the term $[D_u]\dot{\mathbf{U}}$. Consequently, the nonlinear forces $\mathbf{F}_{NL}$ are independent of $\dot{\mathbf{U}}$ and therefore, depend only on $\mathbf{U}$. The $(n_u \times n_u)$ symmetric positive-definite matrix $[M_u]$ is the structural mass matrix. The $(n_u \times n_u)$ symmetric positive-definite matrices $[K_u]$ and $[D_u] = \tau_S\,[K_u]$ are the stiffness and damping matrices of the structure. The rectangular $(n_u \times n_p)$, $(n_h \times n_p)$, and $(n_h \times n_u)$ matrices $[C_{pu}]$, $[C_{p\eta}]$, and $[C_{\eta u}]$ are the coupling matrices between the fluid and the structure, between the fluid and the free surface, and between the structure and the free surface. In Eq.(16) the $\mathbb{R}^{n_u}$-vector $\mathbf{F}_u$ corresponds to the discretization of the external force field applied on the structure. The $\mathbb{R}^{n_u}$-vector $\mathbf{F}_{NL}(\mathbf{U})$ is the discretization of the nonlinear conservative internal forces induced by the geometrical nonlinearities of the structure.

The numerical solution of the nonlinear coupled differential equations (Eq. (14) to (16)) appears to be expensive or even impossible for large finite element models. It is thus essential to introduce an efficient adapted reduced-order model as we have explained in Section 1.

2.3. Construction of the nonlinear reduced-order computational model

The admissible space $\mathcal{C}_{P,H,U}$ is decomposed in the following direct sum,

$$\mathcal{C}_{P,H,U} = \mathcal{C}_P \oplus \mathcal{C}_H \oplus \mathcal{C}_U\,, \tag{17}$$

where the admissible spaces $\mathcal{C}_P$, $\mathcal{C}_H$ and $\mathcal{C}_U$ are defined as follows.

Vector basis of $\mathcal{C}_P$. The admissible space $\mathcal{C}_P$ is related to the conservative part of the discretized problem in $\mathbf{P}$ (see Eq. (14)) for which a zero Neumann boundary condition for the pressure is applied on Γ_L and a zero Dirichlet boundary condition for the pressure is applied on $\Gamma \cup \gamma$. Therefore, a vector basis of $\mathcal{C}_P$ can be constructed as the *acoustic modes*, which are the eigenvectors of the generalized eigenvalue problem (in which the boundary conditions have to be added),

$$[K]\,[\Phi_P] = [M]\,[\Phi_P]\,[\Lambda_P]\,. \tag{18}$$

In Eq. (18), $[\Phi_P] = [\boldsymbol{\varphi}_p^1, \ldots, \boldsymbol{\varphi}_p^{N_P}]$ is the $(n_p \times N_P)$ real matrix whose N_P columns are constituted of the eigenvectors associated with the N_P first smallest positive eigenvalues sorted by increasing order such that $\lambda_p^1 \leq \ldots \leq \lambda_p^{N_P}$ contained

in the diagonal matrix $[\Lambda_P]$.

Vector basis of $\mathcal{C}_H$. The admissible space $\mathcal{C}_H$ is related to the conservative part of the discretized problem in $\mathbf{H}$ (see Eq. (15)) for which the liquid is considered as an inviscid incompressible liquid, with sloshing and capillarity, and for which a zero Neumann boundary condition for the pressure is applied on Γ_L. Therefore, a vector basis of $\mathcal{C}_H$ can be constructed as the *sloshing modes* of the liquid in presence of capillarity, which are the eigenvectors of the generalized eigenvalue problem (in which the boundary condition have to be added),

$$[K]\,[\Phi_{PH}] + [C_{p\eta}]^T\,[\Phi_H]\,[\Lambda_H] = 0\,, \tag{19}$$

$$[C_{p\eta}]\,[\Phi_{PH}] + [K_{gc}]\,[\Phi_H] = 0\,. \tag{20}$$

In Eqs.(19) and (20), $[\Phi_H] = [\boldsymbol{\varphi}_h^1, \ldots, \boldsymbol{\varphi}_h^{N_H}]$ and $[\Phi_{PH}] = [\boldsymbol{\varphi}_{ph}^1, \ldots, \boldsymbol{\varphi}_{ph}^{N_H}]$ are the $(n_h \times N_H)$ and the $(n_p \times N_H)$ real matrices whose N_H columns are constituted of the eigenvectors associated with the N_H first smallest positive eigenvalues sorted by increasing order such that $\lambda_h^1 \leq \ldots \leq \lambda_h^{N_H}$ contained in the diagonal matrix $[\Lambda_H]$.

Vector basis of $\mathcal{C}_U$. The admissible space $\mathcal{C}_U$ is related to the conservative and homogeneous linear part of the discretized problem in $\mathbf{U}$ (see Eq. (16)) related to the structure coupled with a liquid that is inviscid and incompressible, with a zero Dirichlet boundary condition for the pressure on $\Gamma \cup \gamma$ (in addition to the Dirichlet condition on Γ_0). Therefore, a vector basis of $\mathcal{C}_U$ can be constructed as the *elastic modes* of the underlying linear structure with the fluid added mass, which are the eigenvectors of the generalized eigenvalue problem

$$[K_u]\,[\Phi_U] = (\,[M_u] + [M_A]\,)\,[\Phi_U]\,[\Lambda_U]\,. \tag{21}$$

In Eq. (21), the $(n_u \times n_u)$ symmetric positive-definite added-mass matrix $[M_A]$ is defined by

$$[M_A] = [C_{pu}]\,[K_*]^{-1}\,[C_{pu}]^T\,, \tag{22}$$

where $[K_*]^{-1}$ denotes the solution in $[P]$ of the linear matrix equation $[K]\,[P] = [I]$ (in which $[I]$ is the identity matrix) for which, each column $\mathbf{P}^j$ of $[P]$ satisfies the constraint $\mathbf{P}^j = 0$ for the dofs related to $\Gamma \cup \gamma$. In Eq. (21), $[\Phi_U] = [\boldsymbol{\varphi}_u^1, \ldots, \boldsymbol{\varphi}_u^{N_U}]$ is the $(n_u \times N_U)$ real matrix whose N_U columns are constituted of the eigenvectors associated with the N_U first smallest positive eigenvalues sorted by increasing order such that $\lambda_u^1 \leq \ldots \leq \lambda_u^{N_U}$ contained in the diagonal matrix $[\Lambda_U]$.

Computational aspects related to the calculation of the bases. For large-scale 3D computational models, solving the three generalized eigenvalue problems with standard algorithms induced major difficulties for mid-power computers. This is the reason why non-standard algorithms have been proposed in (Akkaoui et al., 2018) for solving these generalized eigenvalue problems. The limitations of the computer resources are principally due to the RAM limitations and a prohibitive CPU time. A double projection method and a subspace iteration method have been proposed and allow for solving such a problem that cannot be treated with standard algorithms.

Reduced-order computational model. The nonlinear reduced-order computational model is constructed by projecting the equations of the fluid-structure system (defined by Eqs. (14) to (16)) on the reduced-order basis $[\Psi]$ constituted of the vector bases constructed above. The solutions $\mathbf{P}$, $\mathbf{H}$, and $\mathbf{U}$ are then written as

$$\begin{bmatrix}\mathbf{P}\\ \mathbf{H}\\ \mathbf{U}\end{bmatrix} = \begin{bmatrix}[\Phi_P] & [\Phi_{PH}] & 0\\ 0 & [\Phi_H] & 0\\ 0 & 0 & [\Phi_U]\end{bmatrix}\begin{bmatrix}\mathbf{q}^p\\ \mathbf{q}^h\\ \mathbf{q}^u\end{bmatrix} = [\Psi]\,\mathbf{Q}\,, \tag{23}$$

in which $\mathbf{Q} = [\mathbf{q}^p\ \mathbf{q}^h\ \mathbf{q}^u]^T$ is the $\mathbb{R}^{N_{phu}}$-vector of the generalized coordinates, with $N_{phu} = N_p + N_h + N_u$, solution of the reduced nonlinear differential equation

$$[\mathscr{M}_{FSI}]\,\ddot{\mathbf{Q}} + [\mathscr{D}_{FSI}]\,\dot{\mathbf{Q}} + [\mathscr{K}_{FSI}]\,\mathbf{Q} + \mathscr{F}_{NL}(\mathbf{Q}) = \mathscr{F}\,, \tag{24}$$

in which the $(N_{phu} \times N_{phu})$ matrices $[\mathscr{M}_{FSI}]$, $[\mathscr{D}_{FSI}]$, $[\mathscr{K}_{FSI}]$, and the $\mathbb{R}^{N_{phu}}$ vector $\mathscr{F}$ are defined as

$$[\mathscr{M}_{FSI}] = [\Psi]^T \begin{bmatrix} [M] & -[C_{p\eta}]^T & -[C_{pu}]^T \\ 0 & 0 & 0 \\ 0 & 0 & [M_u] \end{bmatrix} [\Psi] \,, \tag{25}$$

$$[\mathscr{D}_{FSI}] = [\Psi]^T \begin{bmatrix} [D] & 0 & 0 \\ 0 & 0 & 0 \\ 0 & 0 & [D_u] \end{bmatrix} [\Psi] \,, \tag{26}$$

$$[\mathscr{K}_{FSI}] = [\Psi]^T \begin{bmatrix} [K] & 0 & 0 \\ [C_{p\eta}] & [K_{gc}] & [C_{\eta u}] \\ [C_{pu}] & [C_{\eta u}]^T & [K_u] \end{bmatrix} [\Psi] \,, \tag{27}$$

$$\mathscr{F} = [\Psi]^T \begin{bmatrix} 0 \\ 0 \\ \mathbf{F}_u \end{bmatrix} . \tag{28}$$

In Eq. (24), $\mathscr{F}_{NL}(\mathbf{Q})$ denotes the nonlinear conservative contribution of the geometrical nonlinearities of the structure. The generalized conservative internal nonlinear forces are written (Mignolet and Soize, 2008) as

$$\mathscr{F}_{NL}(\mathbf{Q}) = \mathscr{K}^{(2)}_{\alpha\beta\gamma}\, q^u_\beta\, q^u_\gamma + \mathscr{K}^{(3)}_{\alpha\beta\gamma\delta}\, q^u_\beta\, q^u_\gamma\, q^u_\delta \,, \tag{29}$$

where the quadratic and cubic stiffness $\mathscr{K}^{(2)}_{\alpha\beta\gamma}$ and $\mathscr{K}^{(3)}_{\alpha\beta\gamma\delta}$ are such that

$$\mathscr{K}^{(2)}_{\alpha\beta\gamma} = \frac{1}{2}\left(\widehat{\mathscr{K}^{(2)}_{\alpha\beta\gamma}} + \widehat{\mathscr{K}^{(2)}_{\beta\gamma\alpha}} + \widehat{\mathscr{K}^{(2)}_{\gamma\alpha\beta}}\right) , \tag{30}$$

$$\widehat{\mathscr{K}^{(2)}_{\alpha\beta\gamma}} = \int_{\Omega_S} a_{ijk\ell}\, \varphi^\alpha_{i,j}\, \varphi^\beta_{m,k}\, \varphi^\gamma_{m,\ell}\, d\mathbf{x} \,, \tag{31}$$

$$\mathscr{K}^{(3)}_{\alpha\beta\gamma\delta} = \frac{1}{2}\int_{\Omega_S} a_{ijk\ell}\, \varphi^\alpha_{s,i}\, \varphi^\beta_{s,j}\, \varphi^\gamma_{m,k}\, \varphi^\delta_{m,\ell}\, d\mathbf{x} \,, \tag{32}$$

The numerical aspects of the generalized nonlinear forces are detailed in (Capiez-Lernout et al., 2012).

3. Simulating the experimental setup with the nonlinear reduced-order computational model

3.1. Experimental setup, computational model, and updating the structural model with experimental eigenfrequencies of the structure in vacuo

The experimental setup is the one described in (Lindholm et al., 1962; Abramson et al., 1966). The structure is a steel tank constituted of a thin circular cylinder closed at both ends by circular plates. Its isotropic material properties are given by $E = 2.05 \times 10^{11}\, N.m^{-2}$, $\nu = 0.29$, $\rho_S = 7\,800\, Kg.m^{-3}$, and damping coefficient $\tau_S = 10^{-6}$. This tank is filled with 30% water with sound velocity $c_0 = 1\,480\, m.s^{-1}$, mass density $\rho_0 = 1\,014\, kg.m^{-3}$, and damping coefficient $\tau = 10^{-5}$.

Since capillarity effects are taken into account in the computational model, a water-steel contact angle of $\theta = 83°$ has been considered to compute the equilibrium position of the free surface of the liquid using the software Surface Evolver (Brakke, 1992). Let $R_e = 3.7833 \times 10^{-2}\, m$ and $R_i = 2.76047 \times 10^{-2}\, m$ be the external and the internal radii of the steel cylinder. The thickness of the end plates and the thickness of the cylindrical shell are $h_d = 2.54 \times 10^{-2}\, m$ and $e = 2.286 \times 10^{-4}\, m$. The total height of the tank and the fluid depth are $h = 0.23876\, m$ and $h_f = 0.3\, h$. The geometry of the computational model is described in Figure 2 (left). The origin O of the Cartesian coordinates system $(O, \mathbf{e}_1, \mathbf{e}_2, \mathbf{e}_3)$ is located at the center of the bottom of the cylindrical tank. Axis $\mathbf{e}_3$ coincides with the revolution axis of the system. A particular attention is paid to the modeling of the boundary conditions of the experimental setup. Thus, the structural node located at the bottom center of the tank is locked along its directions $\mathbf{e}_1$, $\mathbf{e}_2$, and $\mathbf{e}_3$. The node

located at the top center of the tank is locked along its directions $\mathbf{e}_1$ and $\mathbf{e}_2$. The rotation of the bottom plate is locked with one dof on the edge of the plate. The boundary conditions described hereinabove (represented by $\circ$ symbol) are displayed in Figure 2 (right figure). Moreover, the experimental pin-ended and cantilever boundary conditions are set in order to study the breathing vibrations of the cylinder. In the present numerical simulation, the structural model in vacuo has been calibrated by optimizing the thickness of the bottom and top plates such that the numerical eigenfrequencies of the structure coincides with the experimental ones. The optimization must take into account the fact that the plates have to stay rigid compared to the cylinder wall. This is why the optimal thickness of these plates has been set as $h_d = 2.54 \times 10^{-3}\, m$.

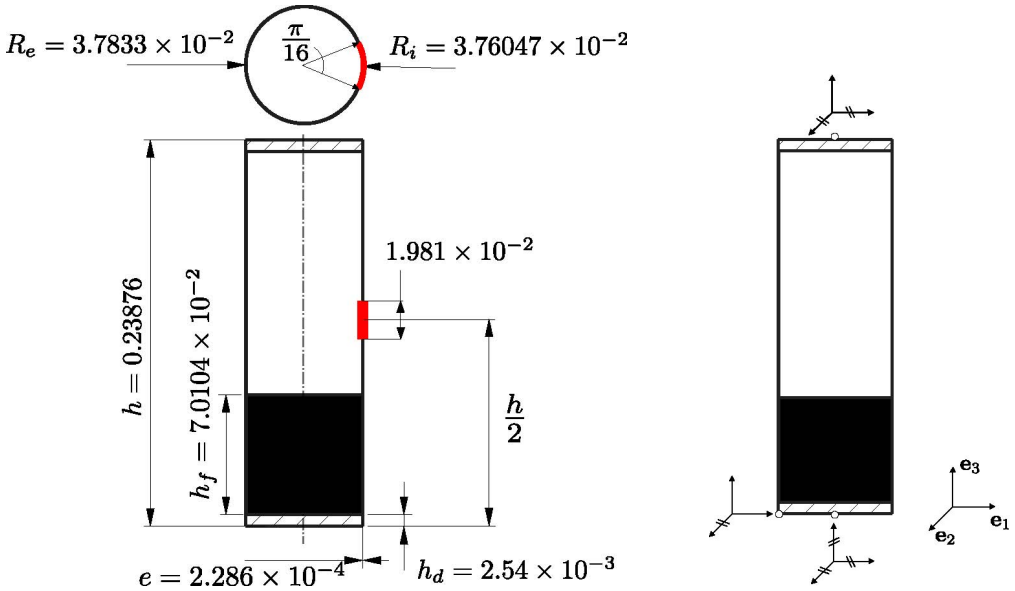

Figure 2: Dimensions of the fluid-structure system (left) and representation of the numerical boundary conditions applied on the system (right).

	Nodes	**Dof**	**Elements**
Fluid	431 354	431 354	296 459
Free surface	11 566	11 566	5 684
Structure	660 385	1 981 155	334 784

Table 1: Table of the finite element mesh properties.

The finite element model of the fluid-structure system is constructed using 3D-solid tetrahedral finite elements with 10 nodes for the structure and for the acoustic fluid (see Figure 3). The free surface of the liquid is meshed using 2D finite elements with 6 nodes and the triple line is meshed using 1D finite elements with 3 nodes. Table 1 sums up the characteristics of the finite element mesh. This high-order finite element modeling is chosen in order to accurately simulate the highly flexible motion of the thin shell and also of the liquid free surface. This choice has been motivated by the fact that there are few difficulties for obtaining correct structural eigenfrequencies and representative sloshing eigenmodes when using linear interpolation functions for finite elements with order 1. Consequently, the finite element mesh is constituted of finite elements with order 2, which allows for accurately representing the dynamical behavior of the system. It is important to note that only the eigenfrequencies are available from the experiments.

Observation points. The dynamical response of the fluid-structure system is analyzed for different observation points of the finite element mesh. These observations points are chosen to be of best interest for the dynamical study of the system. One of them is common to both the structure, the fluid, and the free surface. It allows for seeing the correspondance between the pressure in the acoustic fluid, the displacement of the structure, and the elevation of the

Figure 3: Finite elements meshes of the structure with 1 981 155 dofs (left figure), of the liquid with 431 354 dofs (right figure), and of the free surface with 11 566 dofs (top of the right figure).

free surface. This common point is denoted as $\mathbf{x}_1^p$ in the fluid, $\mathbf{x}_1^h$ on the free surface, and $\mathbf{x}^u$ on the structure. Moreover, another observation point $\mathbf{x}_2^p$ is the point located at the bottom of the fluid is also chosen. Finally, another observation point $\mathbf{x}_2^h$ is also chosen as the point located at the center of the free surface. For the sake of clarity, the coordinates of these observation points are summarized in Table 2. The quantities P_i and H_i denote the pressure and the elevation of the free surface at observation points $\mathbf{x}_i^p$ and $\mathbf{x}_i^h$ (for $i = 1, 2$), and U_j is the component j (for $j = 1, 2, 3$), of the structural displacement at observation point $\mathbf{x}^u$.

Location	Name	x coordinate	y coordinate	z coordinate
Fluid	$\mathbf{x}_1^p$	0.0187	0	0.0076
	$\mathbf{x}_2^p$	0.0187	0	0.0708
Free surface	$\mathbf{x}_1^h$	−0.0144	−0.0347	0.1248
	$\mathbf{x}_2^h$	0	0	0.1245
Structure	$\mathbf{x}^u$	−0.0144	−0.0347	0.1248

Table 2: Coordinates of the observation points for the fluid, the structure and the free surface

3.2. Dynamical excitation of the system

The dynamical excitation is a time-dependent force for which its Fourier transform is a constant in the frequency band of excitation $\mathbb{B}_e = [\nu_{min}, \nu_{max}]\,Hz$, with $\nu_{min} = 500\,Hz$ and $\nu_{max} = 2\,500\,Hz$. The nonlinear responses is computed in the time domain. The Fourier transform of the time response allows for obtaining the response in the frequency domain. The external load vector, which was denoted by $\mathbf{F}_u$, is written as

$$\mathbf{F}_u = \alpha\, g(t)\, \mathbf{F} \quad , \tag{33}$$

in which α is the intensity coefficient taken as $\alpha = 4$, $g(t)$ is the time function of the dynamical excitation, and $\mathbf{F}$ is the normalized vector representing the spatial distribution of the external time load. The excitation is located on a small rectangular patch, which is radially oriented (see the red patch in Figure 2 left). In Eq. (33), the signal $g(t)$ is written as

$$g(t) = 2\Delta\nu\, \mathrm{sinc}_\pi(\Delta\nu\, t)\, \cos(2\pi\, s\, \Delta\nu\, t) \quad , \tag{34}$$

in which $\Delta\nu = \nu_{max} - \nu_{min}$, $s = \dfrac{\nu_{max} + \nu_{min}}{2\Delta\nu}$, and $\mathrm{sinc}_\pi(x) = \dfrac{\sin(\pi\, x)}{\pi\, x}$. Therefore, the Fourier transform of $g(t)$ is written as

$$\widehat{g}(2\pi\nu) = \mathbb{1}_{\mathbb{B}_e}(\nu) \quad , \tag{35}$$

which is 1 if $\nu \in \mathbb{B}_e$ and 0 otherwise. The main computational difficulty is to well capture the very low-frequency sloshing modes of the free surface. Consequently, the time duration of the response computation has to be sufficiently high for obtaining a good frequency resolution and to be such that the response at the final time corresponds to the static equilibrium. The computation is carried out on a truncated time domain $[t_{ini},\, t_{ini} + T]$ with a long time duration T for which $t_{ini} = -1.28\,s$ and $T = 21\,s$. The sampling frequency and the number of time steps are chosen as $\nu_e = 25\,000\,Hz$ and $N_t = 524\,288$.

3.3. Computation of the reduced-order bases

The computation of the reduced-order bases is performed by solving the generalized eigenvalue problems presented in Section 2.3. The computed elastic, acoustic, and sloshing-capillarity modes are indexed by their eigenfrequencies denoted by $\nu_i^a = (\lambda_i^a)^{1/2}/2\pi$, for $i = 1, \ldots, N_a$ with $a \in \{p, h, u\}$.

Acoustic modes. Figure 4 displays four acoustic modes (rank 1, 4, 9, and 15) of the liquid with their respective eigenfrequencies. It should be noted that the fundamental frequency of the internal liquid is $\nu_1^p = 5\,194\,Hz$. Note that this first acoustic eigenfrequency is much greater than the upper bound of the frequency band of excitation.

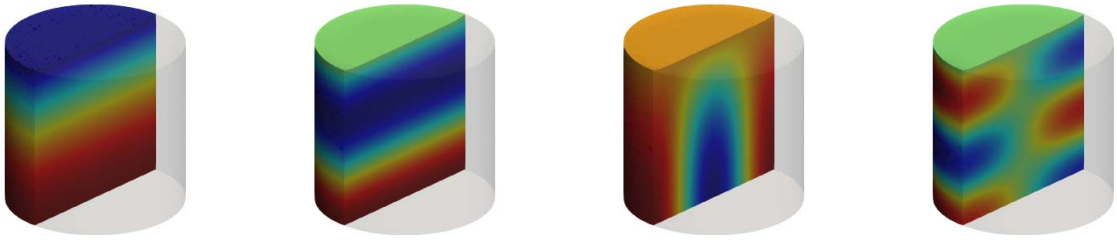

$\nu_1^p = 5\,194\,Hz$ $\nu_4^p = 15\,581\,Hz$ $\nu_9^p = 24\,240\,Hz$ $\nu_{15}^p = 28\,327\,Hz$

Figure 4: Example of acoustic modes of the liquid

Sloshing modes. Figure 5 (upper figure) displays four sloshing modes (rank 1, 20, 25, and 107) of the liquid free surface taking into acount the capillarity effects. It is shown that the fundamental frequency of the free surface is $\nu_1^h = 3.44\,Hz$, that is of order 10^3 smaller than the fundamental frequency of the internal liquid. Moreover, one can see that the modal density of the sloshing phenomena is significant since $\nu_{107}^h = 19.67\,Hz$. The acoustic part of the

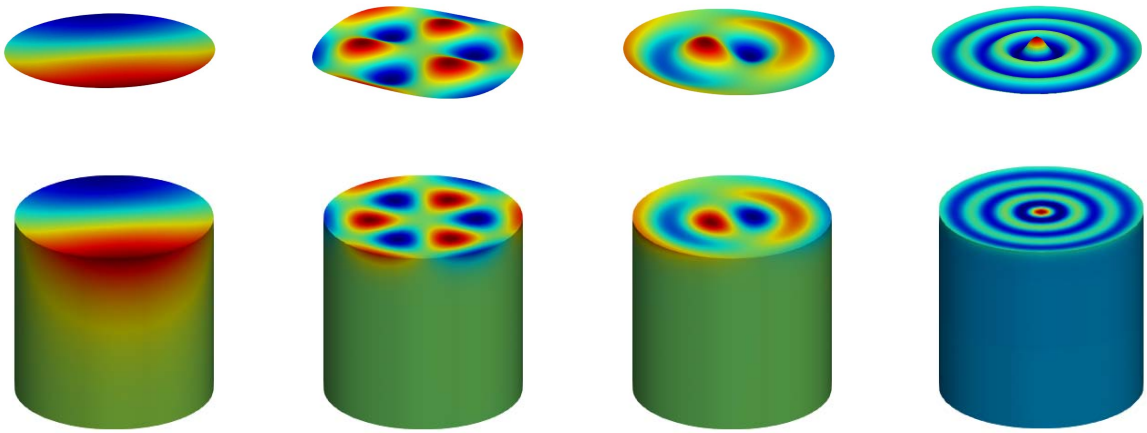

$\nu^h_1 = 3.44\,Hz$ $\nu^h_{20} = 8.28\,Hz$ $\nu^h_{25} = 8.71\,Hz$ $\nu^h_{107} = 19.67\,Hz$

Figure 5: Example of 4 sloshing eigenmodes of the free surface (top) and the corresponding pressure in the acoustic liquid (bottom).

sloshing eigenmodes in the liquid are displayed in Figure 5 (lower figure), for which we can see that the pressure exponentially decreases with respect to the depth of the liquid, as it was expected.

Structural modes with added mass effects. The geometry of the structure has preliminarily been updated in order to match, for the best, the experimentally measured eigenfrequencies for the structure in vacuo. Figure 6 quantifies this updating and displays the graph of the structural eigenfrequencies of the structure in vacuo with respect to the longitudinal and circumferential wave numbers m and n. It should be noted that all the calculations have been carried with the 3D computational model and that the longitudinal and circumferential wave numbers of the structural modes have been identified from the 3D calculations (note that the identification of the values of n and m has been done by examining the 3D plots of the modes). It must also be noted that, in the reduced-order model, all the structural modes have been taken into account in the frequency band: the structural modes $n = 0$ and all the modes $n \geq 1$ for which their eigenfrequencies have a multiplicity greater that one (due to the symmetries). The updated computed structural eigenfrequencies are displayed in blue solid line and the experimental ones (Lindholm et al., 1962) in red triangles. One can see that the updated computational model correctly fits the experimental eigenfrequencies. Concerning the structural modes for which no experiments are available, we have only the computed structural modes. Figure 7 displays two structural modes (rank 6 and 12) in vacuo (two left figures) and displays the corresponding two structural modes (rank 6 and 10) with the added mass effect involved by the liquid for the structure filled with 30% water (two right figures). It is shown that the presence of the liquid locally modifies the in vacuo structural modes in the spatial area where the liquid is in contact with the structure. A decrease of its structural eigenfrequencies is observed (as expected). It should be noted that the structural modes could be constructed for the structure in vacuo. Nevertheless, for this elastic tank partially filled with water, the use of the structural modes computed with the effects of the added mass, yields a much faster speed of convergence of the reduced-order model with respect to the truncation order. Concerning the structural modes in vacuo identified as $n = 0$, the rank of the first one is 89 and its eigenfrequency is $4\,509\,Hz$. The rank of the corresponding structural mode with the added mass effects is 32 and its eigenfrequency is $1\,852\,Hz$ (there is an important shift due to the added mass). It can be seen that this first $n = 0$ structural mode with added mass effects has an eigenfrequency that belongs to the frequency band of excitation. There is no other $n = 0$ structural mode with added mass effects whose rank is less than or equal to 100.

3.4. Eigenfrequency characterization of the system in the frequency band of analysis $\mathbb{B}_a$

Physically there are sloshing modes in the frequency band of excitation $\mathbb{B}_e$ but their contributions in this band $\mathbb{B}_e$ are negligible. Consequently, only the sloshing modes whose eigenfrequencies are below $500\,Hz$ are kept for constructing the ROM. Note that the sloshing eigenfrequencies increase at a very slow rate since $\nu^h_{500} = 57.78\,Hz$. The first

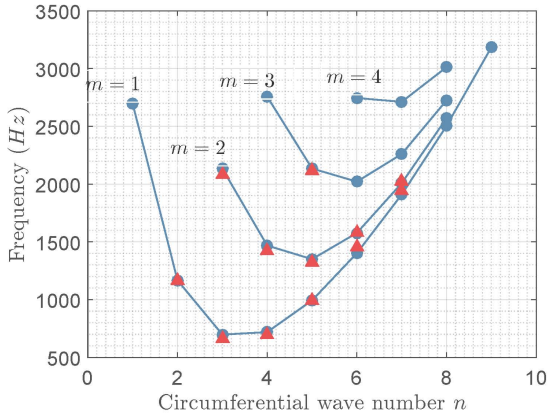

Figure 6: Graph of the structural eigenfrequencies in vacuo calculated with the updated computational model (blue solid line) compared with the experimental eigenfrequencies (red triangles).

$\nu^u_6 = 993\,Hz$ $\nu^u_{12} = 1\,402\,Hz$ $\nu^u_6 = 683\,Hz$ $\nu^u_{10} = 874\,Hz$

Figure 7: Two structural modes (rank 6 and 12) in vacuo (two left figures) and the corresponding two structural modes (rank 6 and 10) with the added mass effect involved by the liquid for the structure filled with 30% water (two right figures)

acoustic mode has an eigenfrequency $\nu^p_1 = 5\,194\,Hz$ greater than the upper bound $2\,500\,Hz$ of $\mathbb{B}_e$. Note that only the the first acoustic eigenfrequency belongs to $\mathbb{B}_a$ since the second acoustic eigenfrequency is $\nu^p_2 = 12\,504\,Hz$. Consequently, only the structural modes occur in the frequency band of the excitation. The eigenfrequency characterization of the fluid-structure system is summarized in Table 3.

Frequency (Hz)	0	500	2 500	6 000
Acoustic			$\nu^p_1 = 5\,194$	
Sloshing	$\nu^h_1 = 3.44$ $\nu^h_{500} = 57.8$			
Structural modes with added mass		$\nu^s_1 = 513$	$\nu^s_{53} = 2\,486$	$\nu^s_{196} = 5\,963$

Table 3: Eigenfrequency characterization of the fluid-structure system

3.5. Solver for computing the nonlinear response in the time domain

The nonlinear coupled differential equation Eq. (24) is solved by using an implicit iterative Newmark scheme for which, at each time step, the nonlinear algebraic equation is solved using the fixed point method or the Newton-Raphson algorithm when the fixed point method is not convergent. Once the time response has been computed, a Fourier transform is performed to analyze the frequency response of the system in the frequency band of analysis $\mathbb{B}_a = [0,\ 6\,000]\,Hz$.

3.6. Convergence of the reduced-order model with respect to the modal truncation

The nonlinear reduced-order model presented in Section 2.3 is constructed using the modes calculated in Section 3.3. A convergence analysis of the nonlinear response is performed with respect to the order of the nonlinear reduced-order model. Since the reference solution cannot be computed for such large-scale nonlinear computational model, it is assumed that the convergence is reached when the response is no longer sensitive to parameters N_p, N_h or N_u. We choose to normalize the convergence function with respect to the solution constructed with $\overline{N}_p = 200$, $\overline{N}_h = 2\,250$, and $\overline{N}_u = 100$. The convergence functions are then defined by,

$$\mathrm{Conv}_{\mathbf{X}}(N_p, N_h, N_u) = \frac{1}{\left\{ \displaystyle\int_{\mathbb{B}_a} |\,\widehat{\mathbf{X}}(\overline{N}_p, \overline{N}_h, \overline{N}_u, 2\pi\nu)\,|^2\, d\nu \right\}^{1/2}} \left\{ \int_{\mathbb{B}_a} |\,\widehat{\mathbf{X}}(N_p, N_h, N_u, 2\pi\nu)\,|^2\, d\nu \right\}^{1/2}, \tag{36}$$

for the Fourier transform $\widehat{\mathbf{X}}$ of a solution $\mathbf{X}$ at a given observation point. Three convergence analyses are then performed with respect to N_p, with respect to N_h, and with respect to N_u. Figure 8 displays the graphs of the following convergence functions,

$$\begin{aligned} N_p &\mapsto \mathrm{Conv}_{\widehat{\mathbf{X}}}(N_p, \overline{N}_h, \overline{N}_u)\,, \\ N_h &\mapsto \mathrm{Conv}_{\widehat{\mathbf{X}}}(\overline{N}_p, N_h, \overline{N}_u)\,, \\ N_u &\mapsto \mathrm{Conv}_{\widehat{\mathbf{X}}}(\overline{N}_p, \overline{N}_h, N_u)\,. \end{aligned} \tag{37}$$

It is shown that the convergence analyses yields an optimal size of the ROM of $N_p = 40$, $N_h = 1\,500$, and $N_u = 60$. It should be noted that the large number of sloshing eigenmodes required for the convergence of the solution is due to the high modal density of the sloshing modes.

Concerning the nonlinear geometrical effect that induces a coupling between displacements of type $n = 0$ and of type $n \geq 1$, the reduced-order model has carefully been constructed and validated by the convergence analysis presented in Section 3.6 for Nu up to 100 (rank of structural modes with added mass effects). The first structural mode with added mass effects, of type n=0, is inside the frequency band of excitation and is kept in the reduced-order model. As the boundary condition of the cylinder at its top end is free in the vertical direction, the structural modes with added mass effects, of type n=0, whose eigenfrequencies are greater than the frequency band of analysis, should a priori be less important.

3.7. Linear and nonlinear dynamical responses of the fluid-structure system

As previously, the notation $\widehat{A}(2\pi\nu)$ denotes the Fourier transform of quantity $A(t)$. The geometrically nonlinear effects induced by the structure are analyzed by comparing the linear and the nonlinear dynamical responses of the system for a given external excitation. For notational convenience, we denote by superscript L the quantities calculated with the linear system and by superscript NL the quantities calculated with the nonlinear system. For $i = \{1, 2\}$, Figure 9 displays the graph of $\nu \mapsto |\widehat{P}_i(2\pi\nu)|$ for the acoustic pressure computed with the linear ROM and with the nonlinear one. First, one can see that numerous resonances arise outside the excitation frequency band $\mathbb{B}_e$ due to the structural nonlinearities. The contributions of most of the elastic modes located above $2\,500\,Hz$ appear in both nonlinear responses. On the other hand, below $500\,Hz$ and for these two observation points, the sloshing modes are not detected due to the exponential decreasing of the sloshing-induced pressure with the depth. In addition, for the nonlinear responses, the resonance peaks located inside $\mathbb{B}_e$ are largely spread out with respect to the ones obtained by the linear responses. This is the case, for example, for the resonance located at $2\,089\,Hz$. For $i = \{1, 2, 3\}$, Figure 10 displays the graph of $\nu \mapsto |\widehat{U}_i(2\pi\nu)|$ for the structural displacement computed with the linear

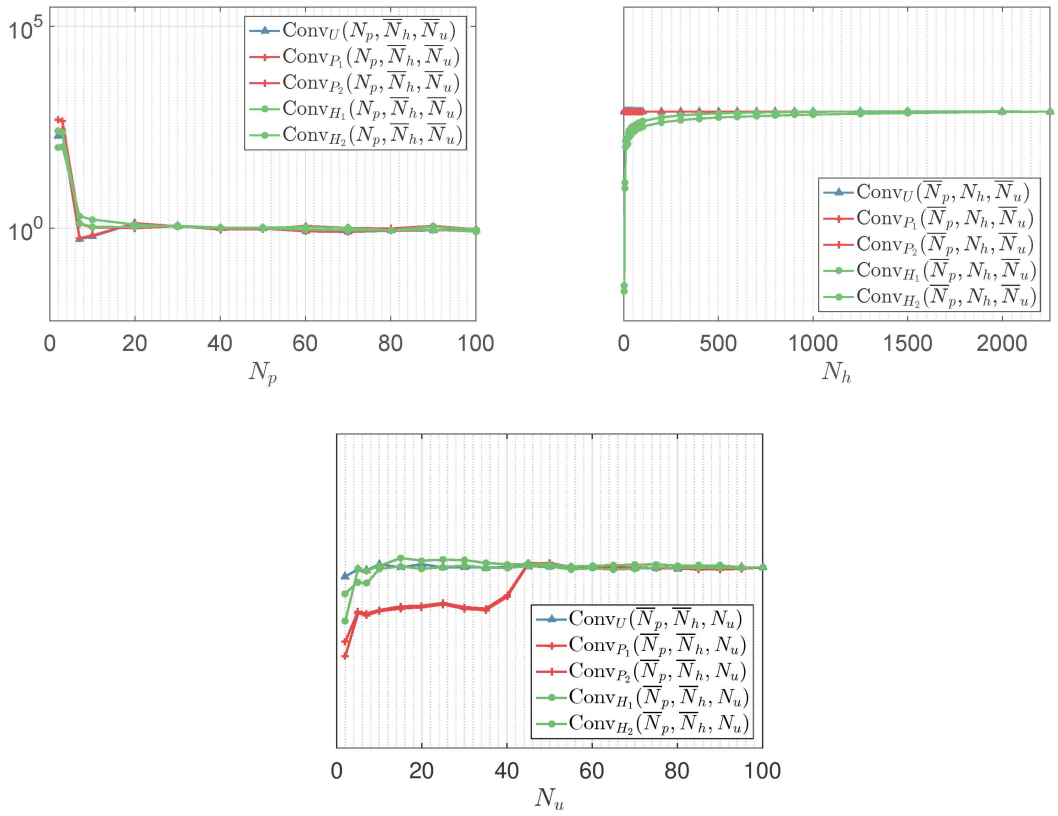

Figure 8: Graph of the convergence functions for **P**, **H**, and **U** at the observation points with respect to N_p (top left), to N_h (top right), and to N_u (down central).

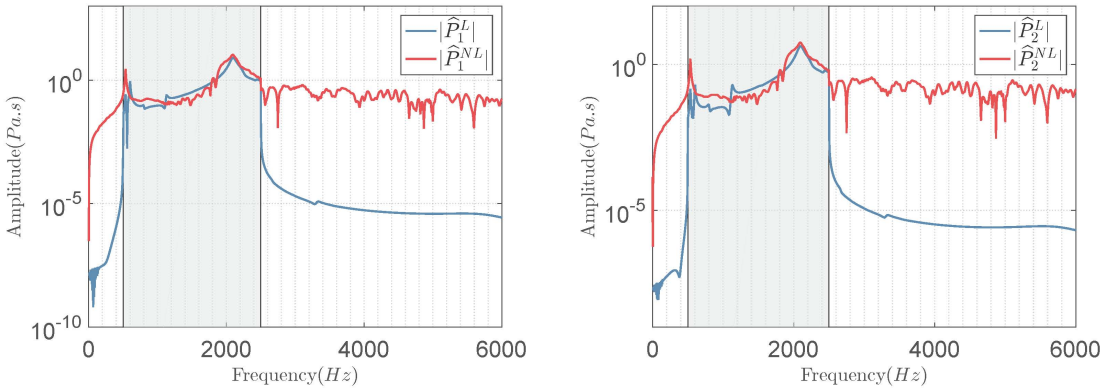

Figure 9: Linear and nonlinear responses of the acoustic pressure. Graphs of $\nu \mapsto |\widehat{P}_1(2\pi\nu)|$ (left) and $\nu \mapsto |\widehat{P}_2(2\pi\nu)|$ (right): pressure computed with the linear ROM (blue line or smooth down grey line for black and white printing) and pressure computed with the nonlinear ROM (red line or irregular top grey line for black and white printing).

ROM and with the nonlinear one. In addition, one can see that some sloshing modes below 500 Hz contribute to the structural displacements. The structural nonlinearities strongly modify the frequency responses in excitation band $\mathbb{B}_e$; the resonance peaks are not only spread out, as for the acoustic pressures, but they are also less isolated and less acute;

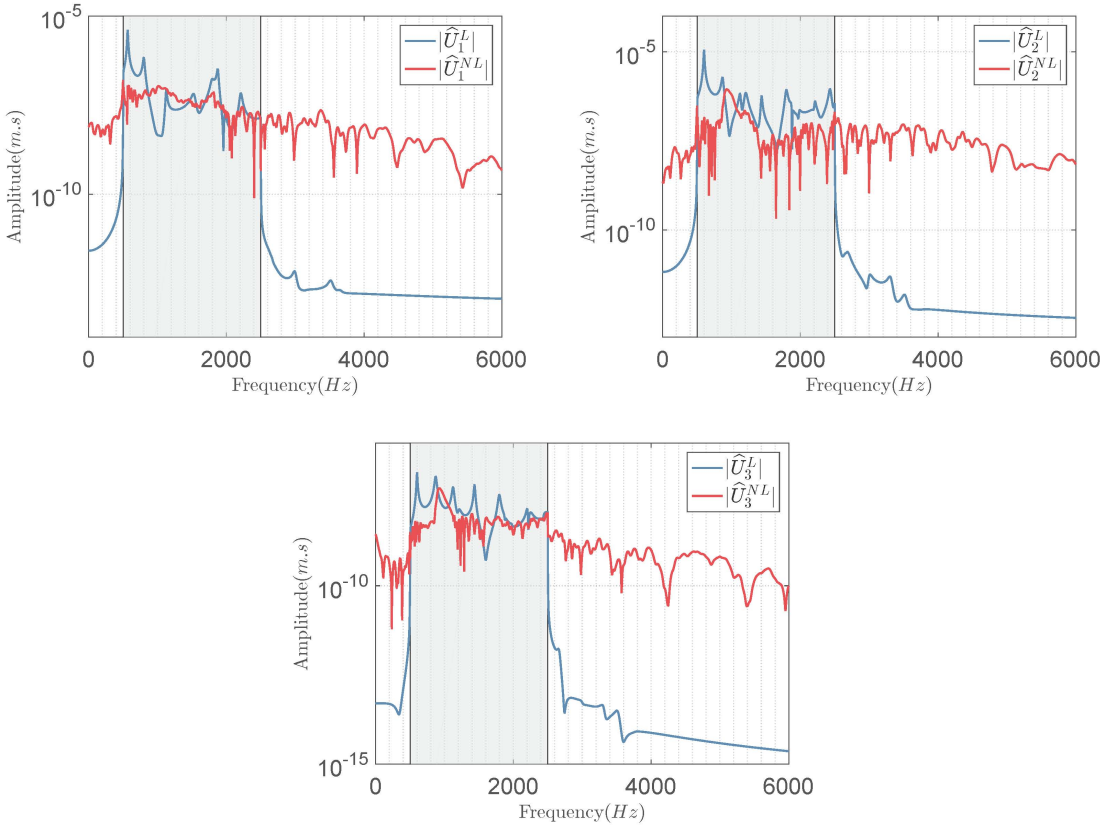

Figure 10: Linear and nonlinear responses for the structural displacement. Graphs of $\nu \mapsto |\widehat{U}_1(2\pi\nu)|$ (top left), $\nu \mapsto |\widehat{U}_2(2\pi\nu)|$ (top right), and $\nu \mapsto |\widehat{U}_3(2\pi\nu)|$ (down central): structural displacements computed with the linear ROM (blue line or relatively smooth down grey line for black and white printing) and structural displacements computed with the nonlinear ROM (red line or irregular top grey line for black and white printing).

this is due to the fact that the energy of the responses in the frequency band $\mathbb{B}_e$ is partially transferred outside this band yielding an apparent damping by this transfer of mechanical energy. The dynamical behavior of the structure is thus significantly damped as it can be seen that the resonances levels inside $\mathbb{B}_e$ are strongly damped by a factor up to 100. Note that the frequency spreading effect is again observed for the resonance located at 872 Hz.

For $i = \{1, 2\}$, Figure 11 displays the graph of $\nu \mapsto |\widehat{H}_i(2\pi\nu)|$ for the free-surface elevation computed with the linear ROM and with the nonlinear one. It can be seen an unexpected response in frequency band $[0\,, 150]\,Hz$ (below the excitation band $\mathbb{B}_e$); the first sloshing modes are excited by the energy transferred in this band, $[0\,, 150]\,Hz$, due to the structural nonlinearities. Let us note that, for the same reasons as the ones given for the structural displacements, an apparent damping by a factor up to 100 occurs in excitation band $\mathbb{B}_e$. In Figure 12, when zooming in the sub-frequency band $[0\,, 150]\,Hz$, one can see that numerous isolated sloshing resonances of high amplitude appear. It is essential to underline that there is a high-amplitude low-frequency free-surface motion while no external excitation exists in this very low-frequency band. The experimental results presented in (Lindholm et al., 1962; Abramson et al., 1966), concerning the unexpected free-surface elevation of liquid in a vibrating cylindrical shell, have been reproduced in the present work that clearly exhibits the same *unexpected phenomena*. The understanding of such complex mechanisms requires to quantify the influence of the different coupling operators involved in the dynamical behavior of the free surface. The investigations that have been done for understanding this phenomenon show that the dynamical response of the free surface is weakly sensitive to the coupling operator $C_{\eta u}$, meaning that the *direct* energy transfer between the structure and the free surface is almost negligible. The complete analysis of this phenomenon is detailed in the next section.

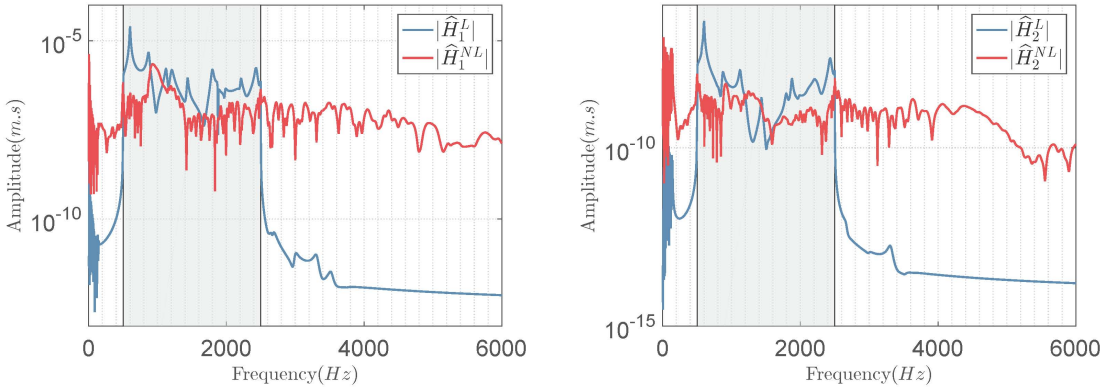

Figure 11: Linear and nonlinear responses for the free-surface elevation. Graphs of $\nu \mapsto |\widehat{H}_1(2\pi\nu)|$ (left) and $\nu \mapsto |\widehat{H}_2(2\pi\nu)|$ (right): free-surface elevation computed with the linear ROM (blue line or relatively smooth down grey line for black and white printing) and free-surface elevation computed with the nonlinear ROM (red line or irregular top grey line for black and white printing).

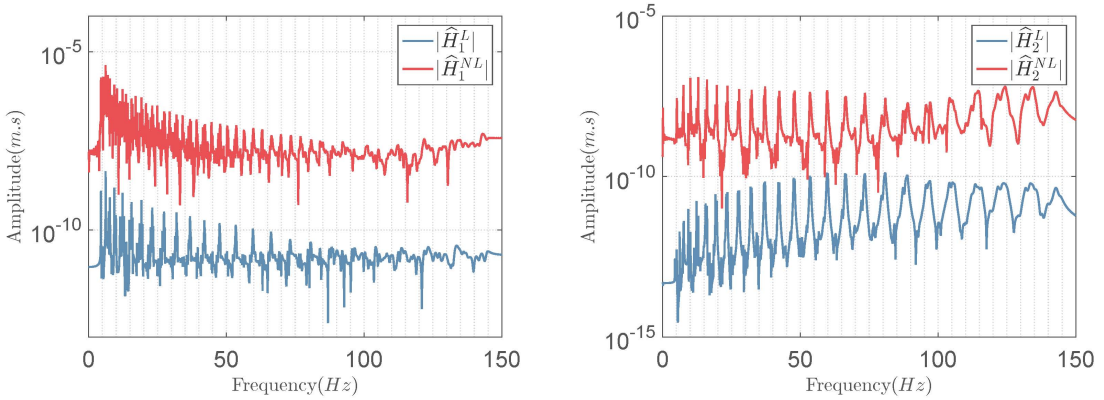

Figure 12: Zoom of the linear and nonlinear responses for the free-surface elevation. Graphs of $\nu \mapsto |\widehat{H}_1(2\pi\nu)|$ (left) and $\nu \mapsto |\widehat{H}_2(2\pi\nu)|$ (right) displayed over the frequency band $[0\,,150]\,Hz$: free-surface elevation computed with the linear ROM (blue line or down grey line for black and white printing) and free-surface elevation computed with the nonlinear ROM (red line or top grey line for black and white printing).

4. Discussion and conclusion

In this paper, we have simulated, using with a large-scale nonlinear computational model, an experimental setup made up of a thin elastic cylinder partially filled with water, for which the available experimental results are limited to the eigenfrequencies of the structure in vacuo but for which unexpected high-amplitude of sloshing phenomenon has been experimentally observed at low-frequency for a high-frequency excitation, which cannot be explained by a linear model. The updated computational model that has been used takes into account the geometrical nonlinearities of the tank, the compressibility of the liquid, the sloshing and the capillarity effects with an adapted contact angle condition. The geometrical nonlinearities of the tank allow for highlighting the phenomenon observed in the experiments.

Considering the numerical results obtained, it appears that the high-amplitude motion of the free surface in the very-low frequency band outside the frequency band of excitation, can be explained by the the couplings illustrated in Figure 13 and explained hereinafter. The geometrical nonlinearities of the structure induce a transfer of the vibrational energy from the high-frequency band of excitation in the very low- and low-frequency band (outside the frequency band of excitation). As the first acoustic modes of the liquid is greater that the upper bound of the high-frequency band of excitation, the acoustic fluid has a quasistatic behavior in the low-frequency band. Therefore, the energy transferred by the structure in the very low-frequency band is transmitted through the acoustic liquid to the first

very low-frequency sloshing modes. This means that the observed phenomenon appears to be an *indirect* transfer of energy from the structure to the free surface through the acoustic liquid and is due to the presence of the geometrical nonlinearity of the elastic tank.

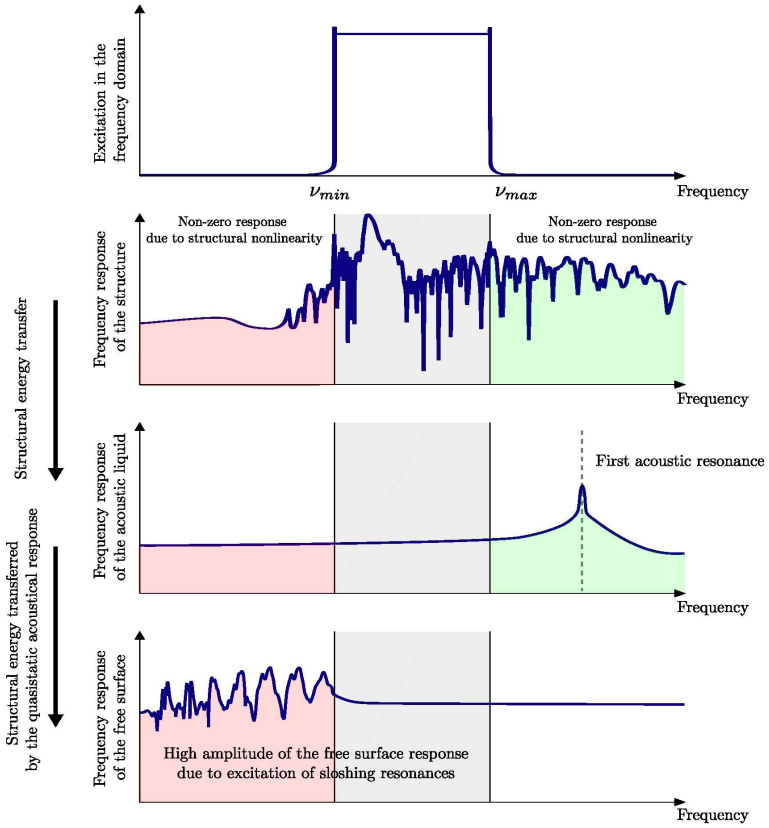

Figure 13: Scheme of the energy transfers between the nonlinear structure, the linear acoustic liquid, and the linear free surface, which explain the excitation of the first sloshing modes in the the very-low frequency band that is outside the frequency band of the external excitations.

Acknowledgements

This work has been partially funded by DGA in France through a PhD grant to the first author.

References

Abramson, H., Kana, D., 1970. Some experimental studies of the dynamic stability of thin shells containing liquid.

Abramson, H., Kana, D., Lindholm, U., 1966. An experimental study of liquid instability in a vibrating elastic tank. Journal of Spacecraft and Rockets 3, 1183–1188.

Akkaoui, Q., Capiez-Lernout, E., Soize, C., Ohayon, R., 2018. Solving generalized eigenvalue problems for large scale fluid-structure computational models with mid-power computers. Computers & Structures 205, 45–54.

Alijani, F., Amabili, M., 2014. Non-linear vibrations of shells: A literature review from 2003 to 2013. International Journal of Non-Linear Mechanics 58, 233–257.

Amabili, M., 2008. Nonlinear vibrations and stability of shells and plates. Cambridge University Press.

Amabili, M., Paıdoussis, M.P., 2003. Review of studies on geometrically nonlinear vibrations and dynamics of circular cylindrical shells and panels, with and without fluid-structure interaction. Applied Mechanics Reviews 56, 349–381.

Amabili, M., Sarkar, A., Paıdoussis, M., 2003. Reduced-order models for nonlinear vibrations of cylindrical shells via the proper orthogonal decomposition method. Journal of Fluids and Structures 18, 227–250.

Amabili, M., Touzé, C., 2007. Reduced-order models for nonlinear vibrations of fluid-filled circular cylindrical shells: comparison of pod and asymptotic nonlinear normal modes methods. Journal of fluids and structures 23, 885–903.

Ballarin, F., Rozza, G., 2016. POD–Galerkin monolithic reduced order models for parametrized fluid-structure interaction problems. International Journal for Numerical Methods in Fluids 82, 1010–1034.
Belytschko, T., Liu, W.K., Moran, B., Elkhodary, K., 2013. Nonlinear finite elements for continua and structures. John wiley & sons.
Bermúdez, A., Rodríguez, R., Santamarina, D., 2003. Finite element computation of sloshing modes in containers with elastic baffle plates. International journal for numerical methods in engineering 56, 447–467.
Brakke, K.A., 1992. The surface evolver. Experimental mathematics 1, 141–165.
Capiez-Lernout, E., Soize, C., Mignolet, M., 2012. Computational stochastic statics of an uncertain curved structure with geometrical nonlinearity in three-dimensional elasticity. Computational Mechanics 49, 87–97.
Carra, S., Amabili, M., Garziera, R., 2013. Experimental study of large amplitude vibrations of a thin plate in contact with sloshing liquids. Journal of Fluids and Structures 42, 88–111.
Chen, J.C., Babcock, C.D., 1975. Nonlinear vibration of cylindrical shells. AiAA Journal 13, 868–876.
Chiba, M., 1992. Nonlinear hydroelastic vibration of a cylindrical tank with an elastic bottom, containing liquid. part i: Experiment. Journal of fluids and structures 6, 181–206.
Chu, W., Kana, D., 1967. A theory for nonlinear transverse vibrations of a partially filled elastic tank. AIAA Journal 5, 1828–1835. doi:10.2514/3.4312.
Crisfield, M.A., Remmers, J.J., Verhoosel, C.V., et al., 2012. Nonlinear finite element analysis of solids and structures. John Wiley & Sons.
Dodge, F.T., 2000. The New Dynamic Behavior of Liquids in Moving Containers. Southwest Resear Institute, San Antonio, Texas.
Dowell, E., 1998. Comments on the nonlinear vibrations of cylindrical shells. Journal of Fluids and Structures 12, 1087–1089.
Faltinsen, O.M., Timokha, A.N., 2009. Sloshing. volume 577. Cambridge University Press Cambridge.
Farhat, C., Chiu, E.K.Y., Amsallem, D., Schotté, J.S., Ohayon, R., 2013. Modeling of fuel sloshing and its physical effects on flutter. AIAA journal 51, 2252–2265.
Finn, R., 2001. On the equations of capillarity. Journal of Mathematical Fluid Mechanics 3, 139–151.
Finn, R., 2006. The contact angle in capillarity. Physics of Fluids 18, 047102.
Finn, R., Luli, G.K., 2007. On the capillary problem for compressible fluids. Journal of Mathematical Fluid Mechanics 9, 87–103.
Hambric, S.A., Sung, S.H., Nefske, D.J., 2016. Engineering Vibroacoustic Analysis: Methods and Applications. John Wiley & Sons.
Ibrahim, R.A., 2005. Liquid Sloshing Dynamics: Theory and Applications. Cambridge University Press, Cambridge.
Koval'chuk, P., Lakiza, V., 1995. Experimental study of induced oscillations with large deflections of fiberglass shells of revolution. International Applied Mechanics 31, 923–927.
Leissa, A.W., 1973. Vibration of shells. volume 288. Scientific and Technical Information Office, National Aeronautics and Space Administration Washington.
Lindholm, U.S., Kana, D.D., Abramson, H.N., 1962. Breathing vibrations of a circular cylindrical shell with an internal liquid. J. Aerospace Sci 29, 1052–1059.
Mignolet, M.P., Soize, C., 2008. Stochastic reduced order models for uncertain geometrically nonlinear dynamical systems. Computer Methods in Applied Mechanics and Engineering 197, 3951–3963.
Moiseyev, N.N., Rumyantsev, V., 2012. Dynamic stability of bodies containing fluid. volume 6. Springer Science & Business Media.
Morand, H.J., Ohayon, R., 1995. Fluid Structure Interaction. John Wiley & Sons, New York.
Ohayon, R., 2004. Reduced models for fluid–structure interaction problems. International Journal for Numerical Methods in Engineering 60, 139–152.
Ohayon, R., Soize, C., 1997. Structural acoustics and vibration: Mechanical models, variational formulations and discretization. Elsevier.
Ohayon, R., Soize, C., 2014. Advanced Computational Vibroacoustics: Reduced-Order Models and Uncertainty Quantification. Cambridge University Press, New York.
Ohayon, R., Soize, C., 2015. Vibration of structures containing compressible liquids with surface tension and sloshing effects. Reduced-order model. Computational Mechanics 55, 1071–1078.
Ohayon, R., Soize, C., 2016. Nonlinear model reduction for computational vibration analysis of structures with weak geometrical nonlinearity coupled with linear acoustic liquids in the presence of linear sloshing and capillarity. Computers & Fluids 141, 82 – 89.
Olson, M.W., 1965. Some experimental observations on the nonlinear vibration of cylindrical shells. AIAA Journal 3, 1775–1777.
Paidoussis, M.P., 1998. Fluid-structure interactions: slender structures and axial flow. volume 1. Academic press.
Schotté, J.S., Ohayon, R., 2005. Incompressible hydroelastic vibrations: finite element modelling of the elastogravity operator. Computers & structures 83, 209–219.
Schotté, J.S., Ohayon, R., 2013. Linearized formulation for fluid-structure interaction: Application to the linear dynamic response of a pressurized elastic structure containing a fluid with a free surface. Journal of Sound and Vibration 332, 2396–2414.
Strand, I.M., Faltinsen, O.M., 2017. Linear sloshing in a 2d rectangular tank with a flexible sidewall. Journal of Fluids and Structures 73, 70–81.
Wriggers, P., 2008. Nonlinear finite element methods. Springer Science & Business Media.
Zienkiewicz, O.C., Taylor, R.L., Zienkiewicz, O.C., Taylor, R.L., 1977. The finite element method. volume 36. McGraw-hill London.